FINAL REPORT

Spatially-Resolved Diagnostics and Modeling of Micro-Discharges
(DE-FG02-03ER54713)

P.I.s: Vincent M. Donnelly and Demetre J. Economou
University of Houston

The goal of this research was to improve our understanding of high pressure DC microdischarge plasmas by a combination of experiments and modeling.

1. Experiments and Modeling of He Micro-discharges

Figure 1.1 shows the geometry of the slot-type microplasma source used in experiments. It consisted of four layers—a top dielectric layer (Al_2O_3), a middle metal layer (Mo), a middle dielectric layer (Al_2O_3), and a bottom layer. The width of the slot was 200 μm. By simply changing the material of the bottom layer and the electrical connections, the microplasma source could be operated in either "hollow cathode discharge mode", or "single cathode discharge mode". The DC electrical connections for a hollow cathode mode are shown in figure 1.2. He discharges were studied.

The discharge was imaged by a set of optical lenses (7X magnification), to the entrance slit of a monochromator. Emission spectra from the plasma region were recorded using a CCD camera. Gas temperature measurements were made by adding small quantities of nitrogen (usually <100 ppm) into the gas feed. The gas temperature was determined from the emission spectra of the second positive system of N_2 ($C^3\Pi_u \rightarrow B^3\Pi_g$).

Spatially resolved measurements of electron temperature were performed using trace rare gas optical emission spectroscopy (TRG-OES). A small amount (<100 ppm) of an equi-mixture of He, Ne, Ar, Kr, and Xe rare gases was added to the He micro-discharge. Emission from Ar, Kr and Xe 2p (Pashen notation) levels was recorded in the 7400-8800 Å range, and Ne 2p emission was recorded in the 5800-7300 Å range.

A one-dimensional, self-consistent fluid model was developed to predict plasma properties, including electron density, electron temperature, gas temperature *etc,* in a parallel plate DC microdischarge at high pressure. The 'single cathode discharge mode' operated in the experiment was treated as a 1-D discharge.

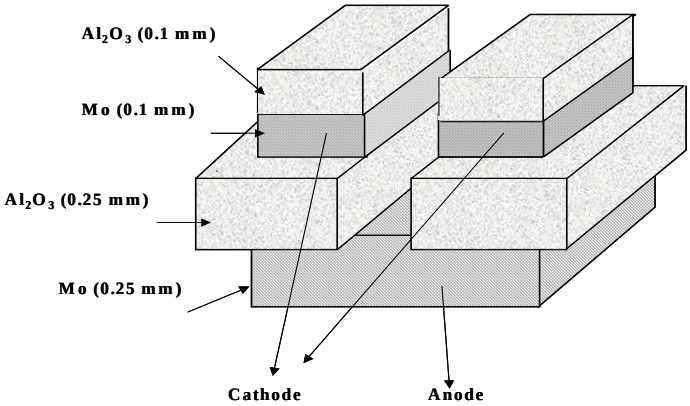

" Hollow cathode configuration"

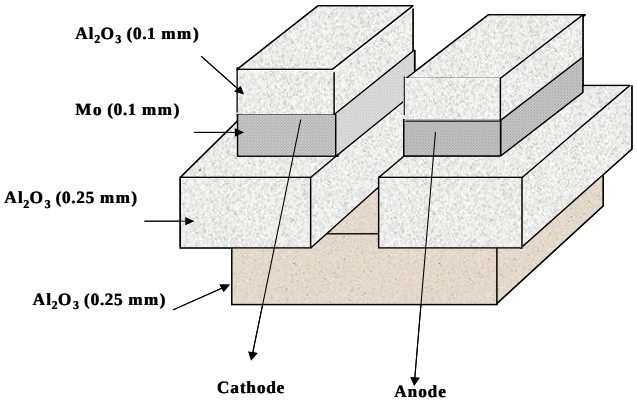

" Single cathode configuration"

Figure 1.1 Geometric configuration of the micro-discharge used in the experiment.

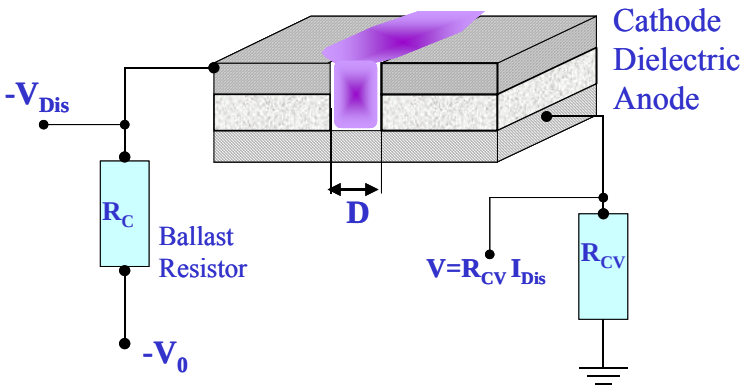

Figure 1.2 Electrical circuit for powering the micro-discharge (hollow cathode mode).

2. Results and Discussion

2.1. Gas temperature measurements

Figure 2.1 shows spectra in the 4620 – 4720 Å spectral range of He micro-discharges with different amounts of added N_2. The helium discharge is very sensitive to impurities, including nitrogen. The presence of nitrogen results in Penning ionization and fast charge transfer reactions. Figure 2.2 shows the I-V characteristics of He micro-discharges at 250 Torr with different amounts of added N_2. The sensitivity of the He discharge to N_2 is evident.

Figure 2.3 presents sample emission spectra of N_2 ($C^3\Pi_u$,0 → $B^3\ \Pi_g$, 0) and N_2 ($C^3\Pi_u$ 1, → $B^3\ \Pi_g$, 0) transitions. Under the discharge conditions of medium pressure (250 Torr) and low current density (250 mA/cm^2), the rotational temperature of N_2 ($C^3\Pi_u$), reflects the gas temperature, which was found to be 354 ± 10 ^{o}C and 359 ± 11 ^{o}C, respectively. The two spectra gave consistent gas temperature. It was also found that the measured gas temperature was almost independent (to within experimental uncertainty) of pressure (in the range of 150 Torr – 600 Torr), and current density (in the range of 100 mA/cm^2 – 400 mA/cm^2). Based on a simple heat transports model, the phenomena can be explained as follows.

The neutral gas temperature T_n (in K) can be computed by

$$\frac{\partial}{\partial t}\left(\frac{3}{2}Nk_BT_n\right) = \nabla(k_n\nabla T_n) + \dot{Q} \tag{1}$$

where N is the gas density, k_n is the thermal conductivity, k_B is Boltzmann's constant, and $\dot{Q}$ is the power density ending up in heating the neutral gas. Boundary conditions are

$$-k_n\frac{\partial T_n}{\partial n} = h(T_n - T_w) \tag{2}$$

where h is a heat transfer coefficient, and T_w is the wall temperature. When Eq. (1) is solved for a 1-D parallel plate geometry (plate separation $2L$) using the symmetry condition at the center ($x=0$) and Eq. (2) on the wall ($x=L$), one obtains steady state solution,

$$T_n = \frac{1}{2}\frac{\dot{Q}L^2}{k_n}(1-(\frac{x}{L})^2) + \frac{\dot{Q}L}{h} + T_w, \tag{3}$$

for a uniform heat generation term $\dot{Q}$. Thus, the gas temperature difference between the center and the wall is

$$\Delta T_n = T_n|_{x=0} - T_n|_{x=L} = \frac{1}{2}\frac{QL^2}{k_n}. \tag{4}$$

The thermal conductivity of He is 1.51x10^{-3} W cm^{-1} K^{-1}. Letting Q=1260 W cm^{-3} (assume 100% of the power is consumed in gas heating, which is an extreme case), and L=0.0125cm (half of the width), the gas temperature different between the center and

wall is simply calculated from Eq. (4). In this case, ΔT is about 65K. If we assume the wall temperature to be 300K (cold wall), then the temperature at the center is about 365K, which is very close to the experiment result.

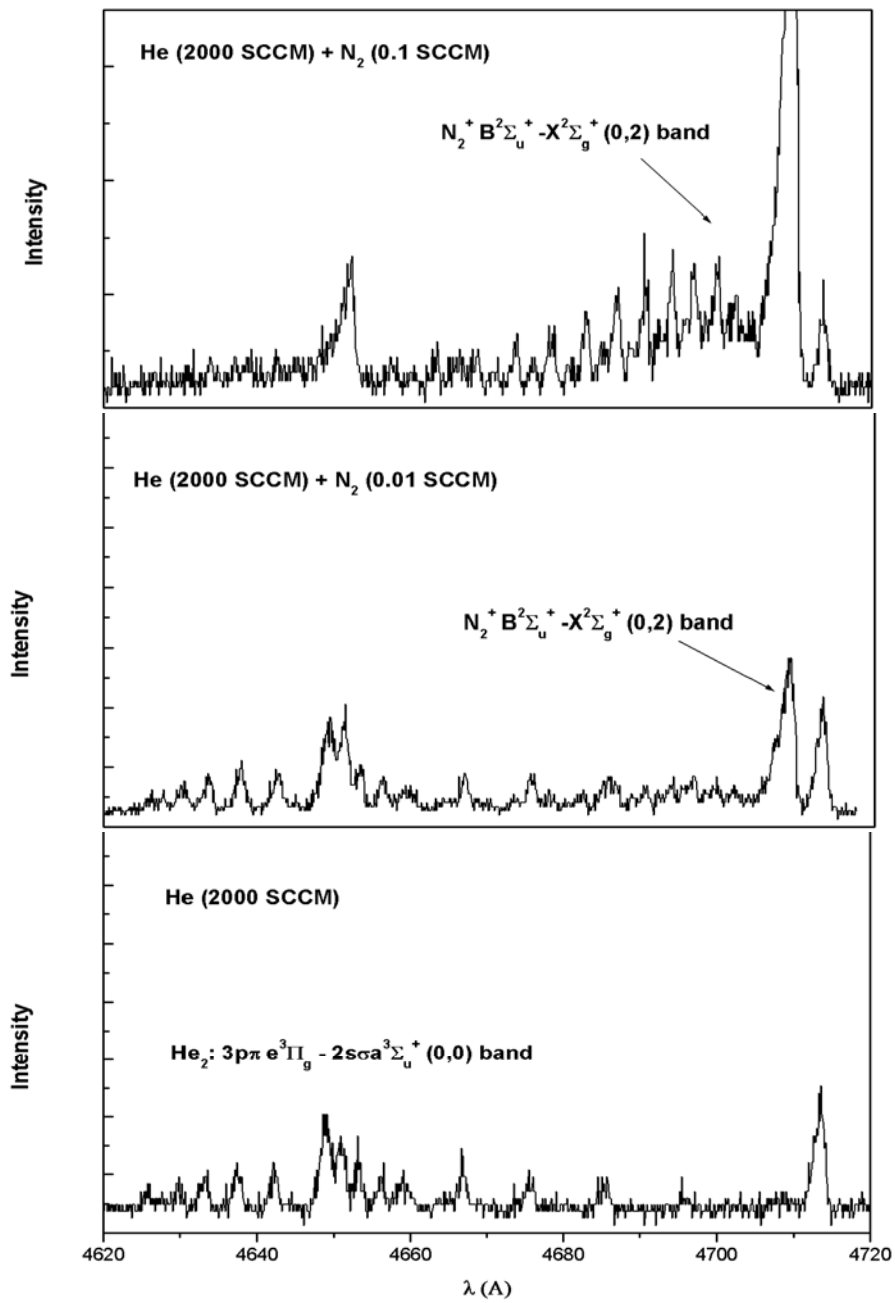

Figure 2.1. Optical emission spectra of He discharges between 4620 and 4720 Å with different amounts of added N_2 (P=250 Torr, I= 250 mA/cm^2).

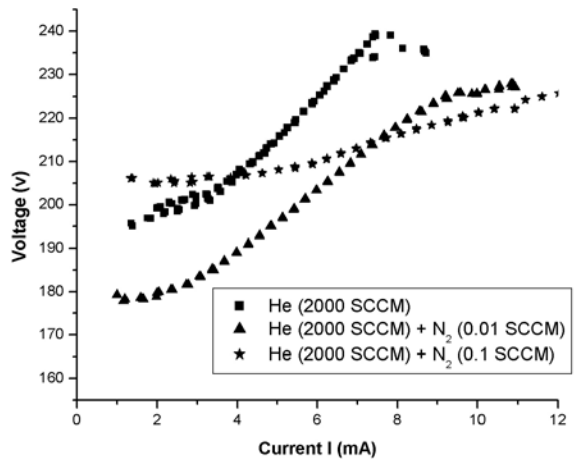

Figure 2.2. DC current-voltage characteristics of He micro-discharges with different amounts of added N_2 (P=250 Torr).

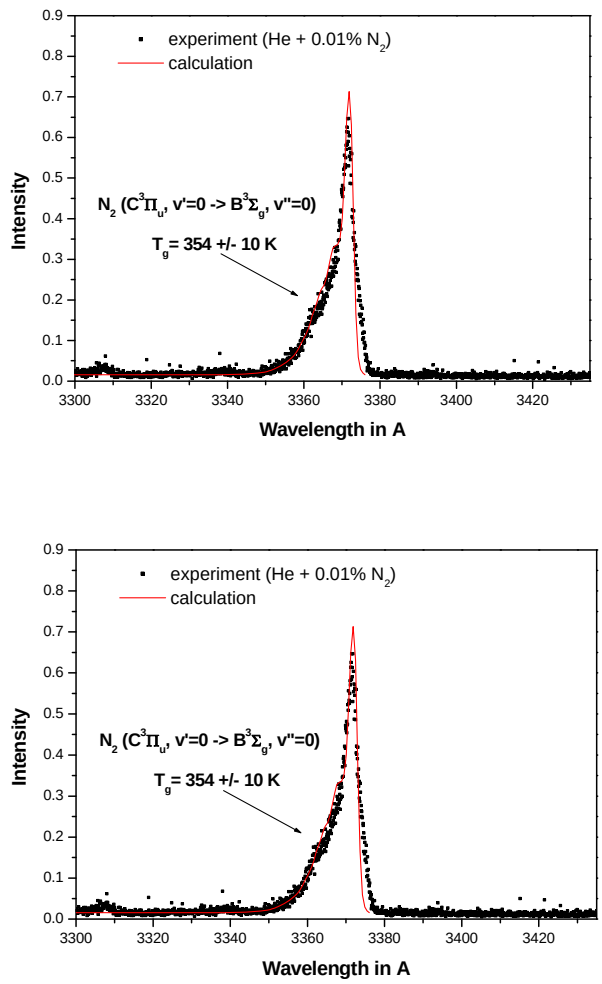

Figure 2.3. Observed and calculated emission spectra of the N_2 ($C^3\Pi_u$,0 → $B^3\ \Pi_g$, 0) and N_2 ($C^3\Pi_u$,1 → $B^3\ \Pi_g$, 0-0) transitions in He micro-discharges at P=250 Torr.

2.2. Electron temperature measurement

Measurements based on TRG-OES are complicated at high pressure, due to the presence of many de-excitation (quenching) processes of excited 2p states. Ion recombination and excitation transfer between He or He_2 metastables and rare gas, which may results in repopulation of the excited states, should also be taken into account.

Figure 2.4 shows the normalized emission intensity profile of the $2p_1 \rightarrow 1s$ transition of Ne, Ar, Kr and Xe in He micro-discharges in 'single-cathode' configuration. The figure represents the spatial distribution of a combination of electron density and temperature. The detected emission intensity, I_A, is given by

$$I_A\,(2p_1 \rightarrow 1s) = f(\alpha(\lambda_{j,k}), Q_b, b_{i,k}, n_{2p1}, T_e) \tag{2.1}$$

$$n_{2p1} = f(n_e, T_e)$$

where $\alpha(\lambda_{i,k})$ is the spectrometer sensitivity at $\lambda_{i,k}$, Q_b is the quantum yield, n_{2p1} is the number density of the $2p_1$ level, n_e is the electron density and T_e is the electron temperature. On the other hand, information on electron temperature alone can be deduced from the emission intensity profile that is normalized to Xe emission (Figure 2.5).

$$\frac{I_A\,(2p1 \rightarrow 1s\ \ Ne,\ Ar,\ or\ \ Kr)}{I_A(2p1 \rightarrow 1s,\ Xe)} = f(T_e....) \tag{2.2}$$

The two figures, taken together, clearly suggest that the electron temperature peaks in the cathode sheath region, while the plasma density peaks away from the cathode sheath. The results are in agreement with results from simulation shown next.

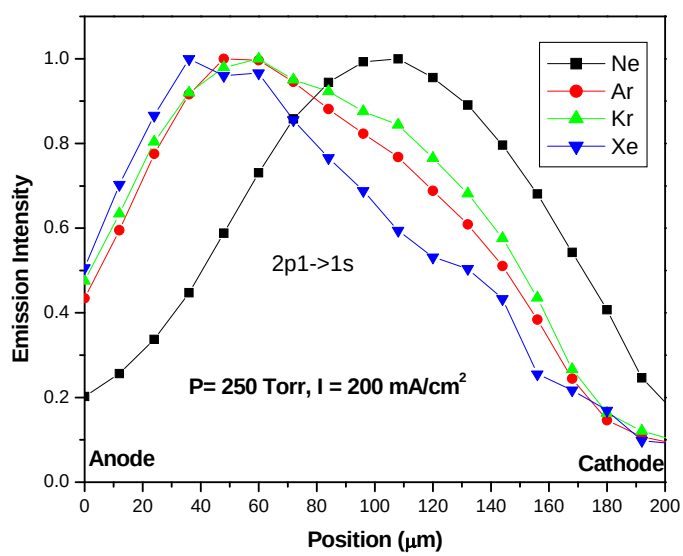

Figure 2.4. Spatially resolved emission intensity of the $2p_1 \rightarrow 1s$ transition of Ne, Ar, Kr and Xe (normalized to its max value) in He micro-discharges in 'single-cathode' configuration.

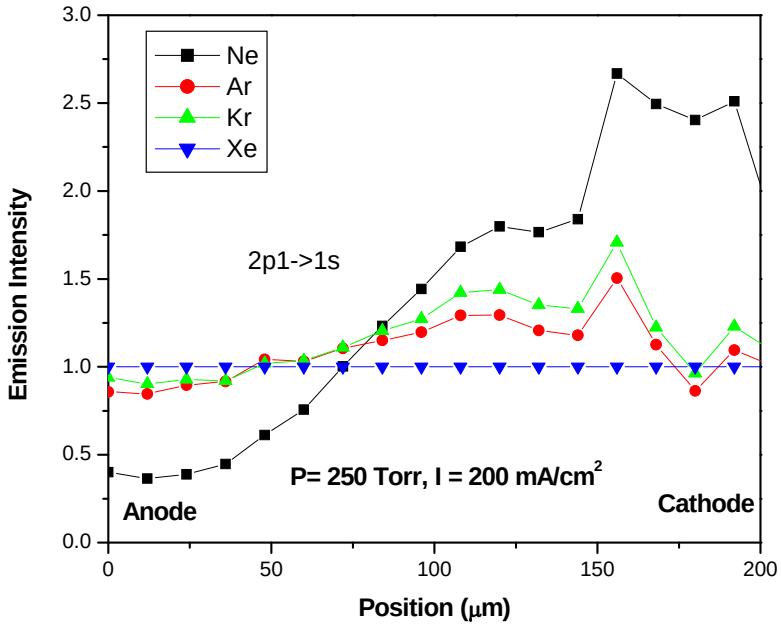

Figure 2.5. Spatially resolved emission intensity of the $2p_1 \rightarrow 1s$ transition of Ne, Ar, Kr and Xe (normalized to Xe emission intensity) in a He micro-discharges in single-cathode configuration.

2.3 1-D micro-discharge simulation

A one-dimensional, self-consistent, fluid model was developed to predict plasma phenomena in a parallel plate DC microdischarge in high pressure He. Basic assumptions included:

(1). The discharged was formed between two large-area parallel conductive electrodes; discharge properties change only along the direction normal to the electrodes.

(2). The particle flux was described by the diffusion/drift approximation. The equations of momentum conservation were not solved. For a gas pressure at ~760 Torr, flow rate ~ 2000 sccm, discharge volume ~ 50 cm^3 (typical experimental conditions), the gas residence time was about 25 ms, which is long compared with metastable diffusion time of ~0.1 ms.

(3). Electrons, atomic ions He^+, molecular ions He_2^+, atomic metastables He*, and molecular metastables He_2* were considered as the main species generated in the discharge. Higher excited states of He and He_2 were not included in the model, due to the very small number density of these excited states.

(4). The electron energy distribution function (EEDF) was assumed to be Maxwellian, and the slow and fast electrons were not treated separately. Thus, an electron temperature equation was solved.

Governing equations included:

(1). <u>Continuity equations</u> for electrons (n_e), atomic ions He^+(n_p), molecular ions He_2^+ (n_{p2}), atomic metastable He* (n*) and molecular metastable He_2* (n_2*)

$$\frac{\partial n_e}{\partial t} + \nabla \cdot J_{ne} = \sum_{ne} R \tag{1}$$

$$\frac{\partial n_p}{\partial t} + \nabla \cdot J_{np} = \sum_{np} R \tag{2}$$

$$\frac{\partial n_{p2}}{\partial t} + \nabla \cdot J_{np2} = \sum_{np2} R \tag{3}$$

$$\frac{\partial n^*}{\partial t} + \nabla \cdot J_{n*} = \sum_{n*} R \tag{4}$$

$$\frac{\partial n_2^*}{\partial t} + \nabla \cdot J_{n_2^*} = \sum_{n_2*} R \tag{5}$$

With the drift-diffusion flux approximation, the flux terms are:

$$J_{ne} = -D_{ne} \nabla n_e + \mu_{ne} n_e \nabla V \tag{6}$$

$$J_{np} = -D_{np} \nabla n_p - \mu_{np} n_p \nabla V, \quad J_{np2} = -D_{np2} \nabla n_{p2} - \mu_{np2} n_{p2} \nabla V \tag{7}$$

$$J_{n*} = -D_{n*} \nabla n_*, \; J_{n_2*} = -D_{n_2*} \nabla n_2^* \tag{8}$$

2). <u>Electron energy balance equation</u>:

$$\frac{\partial}{\partial t}(\frac{3}{2} n_e T_e) = -\nabla \cdot q_{ne} + e J_{ne} \cdot \nabla V - \sum_{ne} \Delta H_j R_j - 3 \frac{m_e}{m_{neut}} n_e v_{me} (T_e - T_g) = 0 \tag{9}$$

The total electron energy flux was given by

$$q_e = -\frac{3}{2} D_e n_e \nabla T_e + \frac{5}{2} T_e J_e \tag{10}$$

3). <u>Poisson Equation</u>:

$$\nabla^2 V = -\frac{e}{\varepsilon_0}(n_p + n_{p2} - n_e) \tag{11}$$

4). <u>Boundary Conditions</u>

On the cathode (@ x = 0)

1). For electrons: $J_{ne} = -k_s n_e - \gamma (J_{np} + J_{np2})$

2). For ions: $J_{np} = -\mu_{np} n_p \nabla V, \; J_{np2} = -\mu_{np2} n_{p2} \nabla V$

3). For metastable species: $n^* = 0, \; n_2^* = 0;$

4). For electron temperture: $T_e = 0.5$

5). For potential: V=0

On the anode (@ x = L)

1). For electrons: $J_e = k_s n_e$

2). For ions: $J_{np} = -\mu_{np} n_p \nabla V, \; J_{np2} = -\mu_{np2} n_{p2} \nabla V$

3). For metastable species: $n^* = 0,\ n_2^* = 0;$

4). For electron temperture: $q_e = \frac{5}{2} T_e J_{ne}$

5). For potential: V= Vp (applied voltage)

In the above equations, n_j , J_j , D_j and μ_j ($j = n_e$, n_p, , n_{p2} , n^* , n_2^*) are particle density, flux, diffusivity, and mobility, respectively. T_e is the electron temperature. V is the potential. Table 1 lists the transport and other parameters that were used in the model.

Table. 1. Parameters values used

	Symbol	Values
Electron diffusivity	D_{ne}	$1.158x10^3 T_e (\frac{760}{P}) cm^2 s^{-1}$
Electron mobility	μ_{ne}	$1.132x10^3 (\frac{760}{P}) cm^2 V^{-1} s^{-1}$
He^+ diffusivity	D_{np}	$5.026x10^{-1} (\frac{760}{P}) cm^2 s^{-1}$
He^+ mobility	μ_{np}	$1.482x10^1 (\frac{760}{P}) cm^2 V^{-1} s^{-1}$
He_2^+ diffusivity	D_{np2}	$8.148x10^{-1} (\frac{760}{P}) cm^2 s^{-1}$
He_2^+ mobility	μ_{np2}	$2.403x10^1 (\frac{760}{P}) cm^2 V^{-1} s^{-1}$
He* diffusivity	D_{n*}	$4.116(\frac{760}{P}) cm^2 s^{-1}$
He_2* diffusivity	D_{n2*}	$2.029(\frac{760}{P}) cm^2 s^{-1}$
Electron recombination coefficient	k_s	$\frac{1}{4}\sqrt{\frac{8eT_e}{\pi m_e}}$
Secondary electron coefficient (on cathode)	r_1	0.01~0.1
Secondary electron coefficient (on anode)	r_2	0

Table 2 lists the reactions that were included in the model. The rate coefficients are also given.

Table 2. Reactions for high pressure helium glow discharge considered in the model.

	Process	Reaction	Rate coefficient	ΔE (eV)
R1	Ground state ionization	He + e → He^+ + 2e	$1.5 \times 10^{-9} (T_e)^{0.68} \exp(-24.6 / T_e)\ cm^3 s^{-1}$	24.6
R2	Ground state excitation	He + e → He* + e	$4.2 \times 10^{-9} (T_e)^{0.31} \exp(-19.8 / T_e)\ cm^3 s^{-1}$	19.8
R3	Step-wise ionization 1	He* + e → He^+ + 2e	$1.28 \times 10^{-7} (T_e)^{0.60} \exp(-4.8 / T_e)\ cm^3 s^{-1}$	4.8
R4	Step-wise ionization 2	He_2*+e → He_2^+ +2e	$9.75 \times 10^{-10} (T_e)^{0.71} \exp(-3.4 / T_e)\ cm^3 s^{-}$	3.4

			1		
R5	Superelastic colliions 1	He* + e → He + e	$2.0 \times 10^{-10} (T_e)^{0.31}$	cm^3s^{-1}	-19.8
R6	Superelastic colliions 2	He_2* + e → 2He + e	$3.8 \times 10^{-9} (T_e/T_g)^{0.25}$	cm^3s^{-1}	-17.9
R7	Metastable Conversion	He* + 2He → He_2* + He	2.0×10^{-34}	cm^6s^{-1}	
R8	Ion conversion	He^+ + 2He → He_2^+ + He	6.42×10^{-32}	cm^6s^{-1}	
R9*	Associate ionization	He**(p>3) + He → He_2^+ +e	8.0×10^{-11}	cm^3s^{-1}	
R10	Metastble-metastable ionization	He* + He* → He^+ + He + e	0.75×10^{-9}	cm^3s^{-1}	-15.0
		→ He_2^+ + e	0.75×10^{-9}	cm^3s^{-1}	-17.4
R11	(Chemoionization)	He* + He_2* → He^+ +2He + e	1.25×10^{-9}	cm^3s^{-1}	-13.1
		→ He_2^+ + e	1.25×10^{-9}	cm^3s^{-1}	-15.5
R12		He_2* + He_2* → He^+ +3 He + e	0.75×10^{-9}	cm^3s^{-1}	-11.3
		→ He_2^+ + e	0.75×10^{-9}	cm^3s^{-1}	-13.7
R13	Recombination of atomic ion (He^+) and electrons	He^+ + e + e → He* + e He^+ + e → He* + hv He^+ + e + He → He* + He	$6.0 \times 10^{-20} (T_e/T_g)^{-4}$	cm^6s^{-1}	
R14	Recombination of molecular (He_2^+) ion and electrons	He_2^+ + e + e → He_2** + e He_2^+ + e → He_2** + hv He_2^+ + e + He → He_2** + He	$4.0 \times 10^{-20} (T_e/T_g)^{-4}$ $4.0 \times 10^{-27} (T_e/T_g)^{-1}$	cm^6s^{-1} cm^6s^{-1}	
R15	Dissociative recombination	He_2^+ + e → He* + He	$5..0 \times 10^{-9} (T_e)^{-0.5}$ or $8.9 \times 10^{-9} (T_e/T_g)^{-1.5}$	cm^6s^{-1}	
R16	Dissociation of He_2*	He_2* → He* + He			

Model results

It is known that DC discharges are mainly sustained by secondary electron emission from the cathode. In the model, the secondary electron emission coefficient was selected as a fitting parameter to match the model predictions to experimental data. Fig.2.6 shows the calculated I-V characteristic curves of the discharge for different values of the secondary electron emission coefficient. The calculated results are shown to be very sensitive to the secondary electron emission coefficient, γ . In the following results, γ was set to 0.05 which best fit the data.

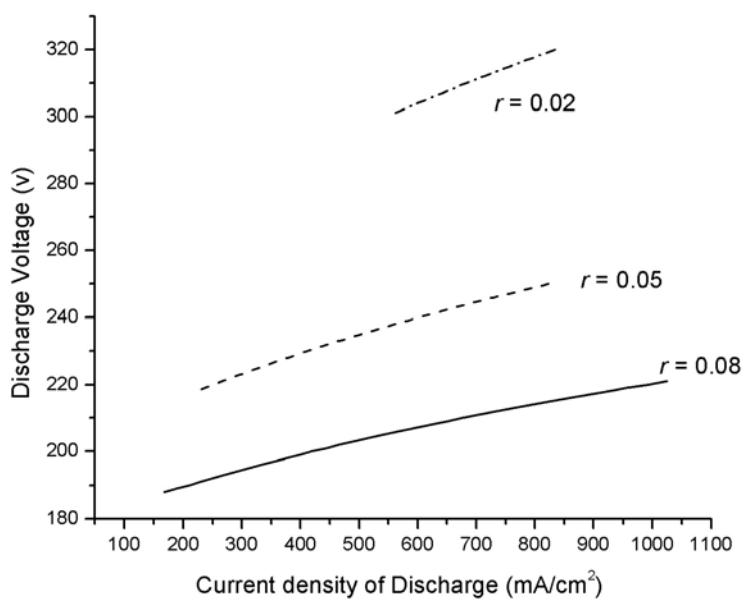

Figure 2.6. Calculated I-V characteristics of He discharges between two parallel plates at P = 250 Torr, d = 250 μm, for different secondary electron emission coefficients (γ).

Figs 2.7-a and 2.7-b present the species density and electron temperature profiles, at P =250 Torr, for the case of relatively high and relatively low current density, respectively. Fig 2.8-a and 2.8-b show the calculated density and temperature profiles at atmospheric pressure. (P=760).

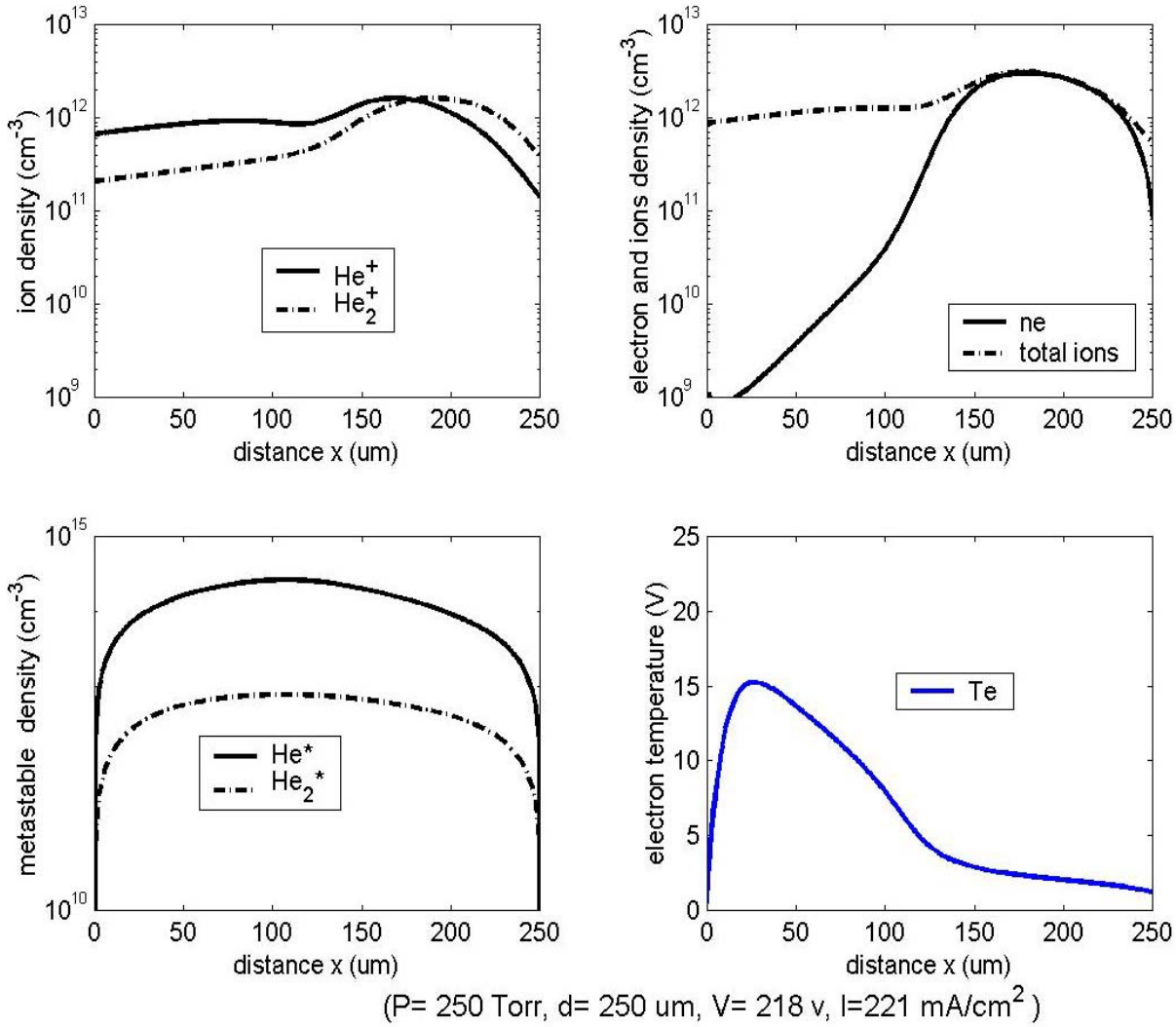

Figure 2.7-a. Electron density, ion density, metastable density and electron temperature profiles at P =250 Torr. (Low current density case: I = 221 mA/cm^2)

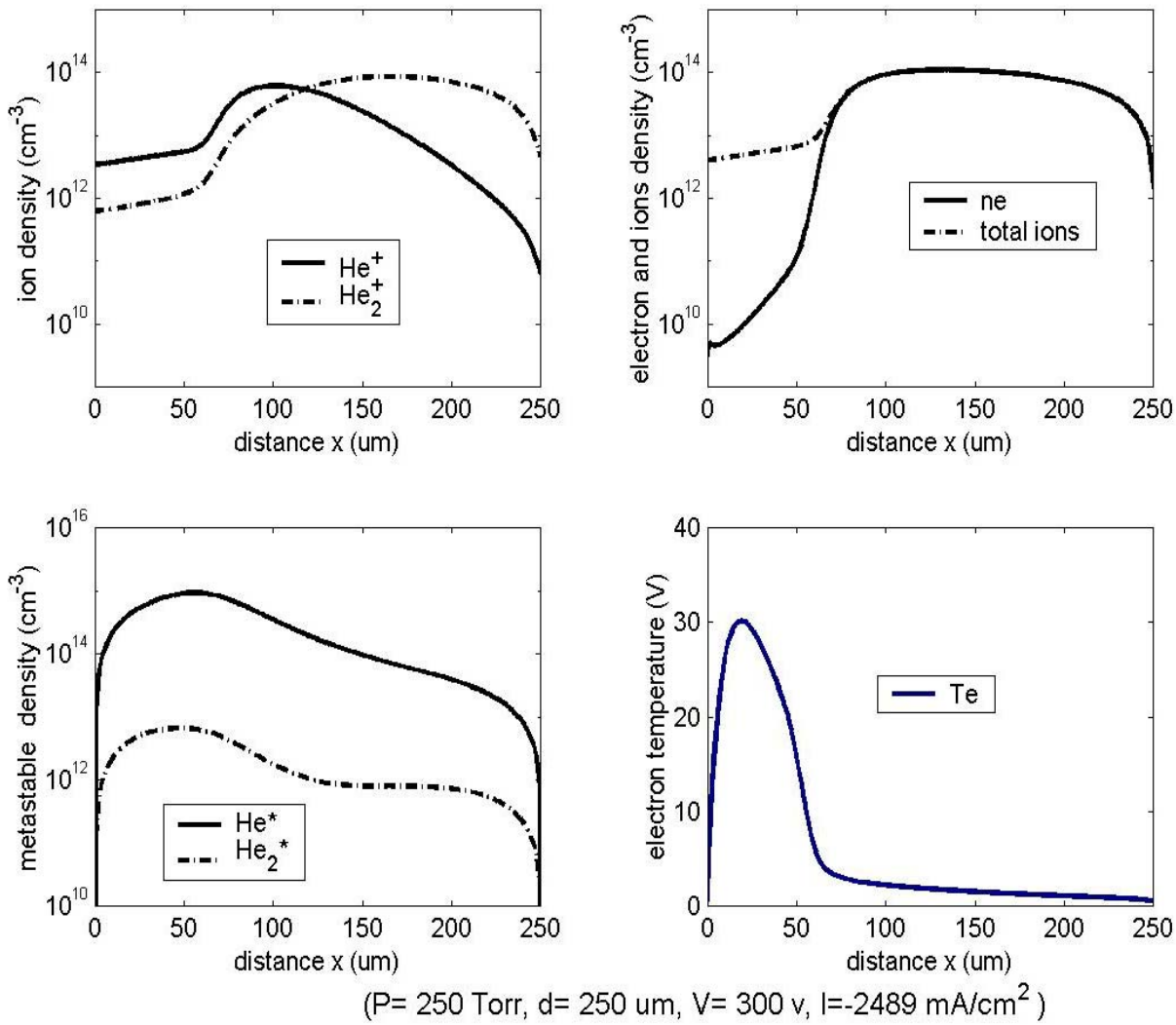

Figure 2.7-b. Electron density, ion density, metastable density and electron temperature profiles at P =250 Torr. (High current density case: I = 2490 mA/cm^2)

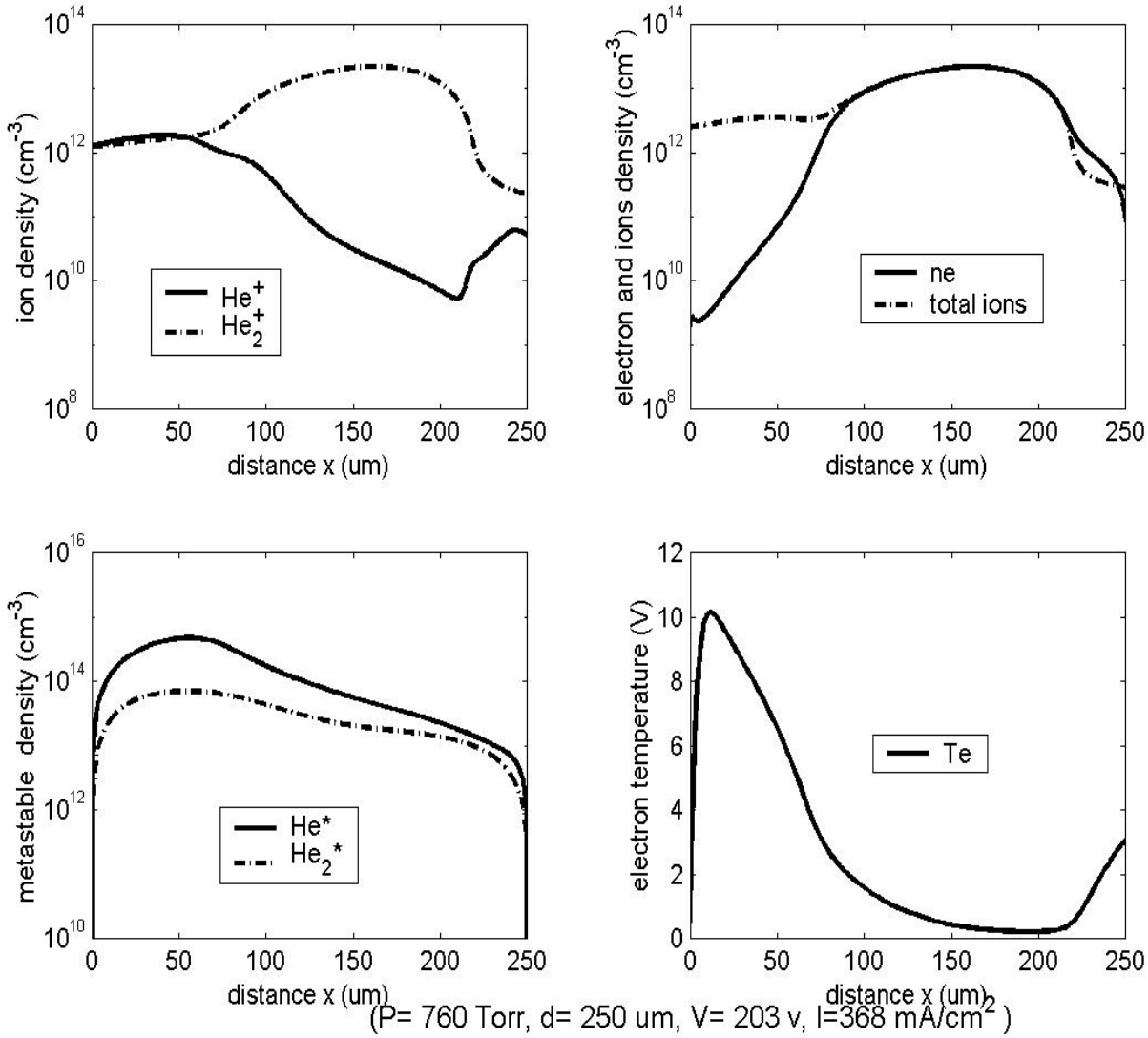

Figure 2.8-a. Electron density, ion density, metastable density and electron temperature profiles at P =760 Torr. (Low current density case: I = 368 mA/cm^2)

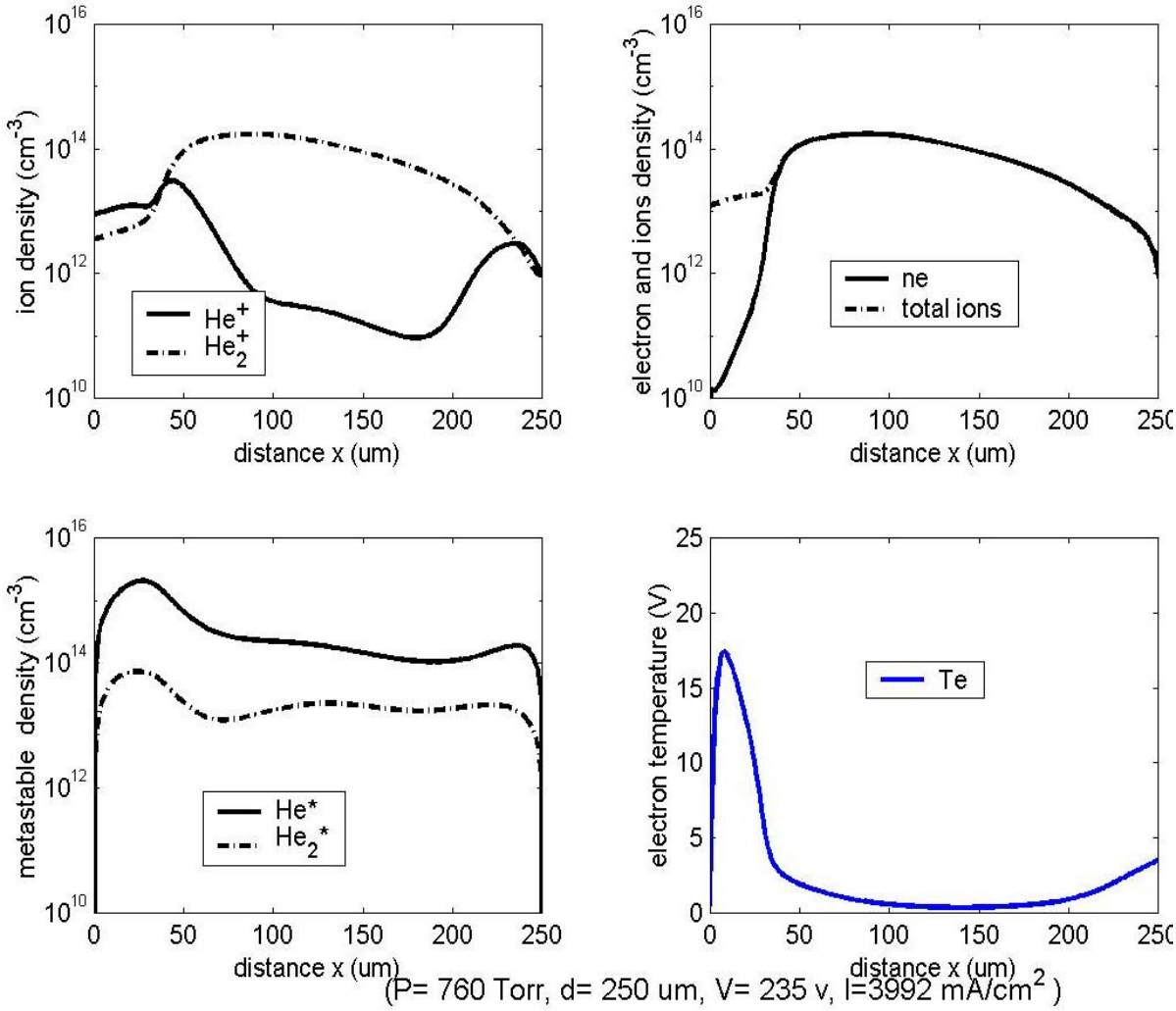

Figure 2.8-b. Electron density, ion density, metastable density and electron temperature profiles at P =760 Torr. (High current density case: I = 3992 mA/cm^2)

Tables 3 and 4 summarize the dominant generation (gain) and loss processes for each species across the discharge (diffusion losses are not listed here). Generally, the higher the pressure, the more likely for three body reactions to dominate. Two-body ionization and electron-impact excitation occur mostly near the region of high electron temperature. It was also found that these dominant processes are not sensitive to discharge current.

Table.3. Dominant loss processes by reaction for electrons, ions and metastables

Species	Discharge Position	P=250 Torr (For both low and high current cases)	P = 760 Torr (For both low and high current cases)
Electron lost	Close to Cathode	He_2^+ + **e** + He → He_2* + He	He_2^+ + **e** + He → He_2* + He
	In the Center	He_2^+ + **e** + He → He_2* + He	He_2^+ + **e** + He → He_2* + He
	Close to Anode	He_2^+ + **e** + He → He_2* + He	He_2^+ + **e** + He → He_2* + He
He^+ lost	Close to Cathode	**He^+** + He + He → He_2^+ + He	**He^+** + He + He → He_2^+ + He
	In the Center	**He^+** + He + He → He_2^+ + He	**He^+** + He + He → He_2^+ + He
	Close to Anode	**He^+** + He + He → He_2^+ + He	**He^+** + He + He → He_2^+ + He
He_2^+ lost	Close to Cathode	**He_2^+** + e + He → He_2*+ He	**He_2^+** + e + He → He_2*+ He
	In the Center	**He_2^+** + e + He → He_2*+ He	**He_2^+** + e + He → He_2*+ He
	Close to Anode	**He_2^+** + e + He → He_2*+ He	**He_2^+** + e + He → He_2*+ He
He* lost	Close to Cathode	**He*** + **He*** (or He_2*) →e + He_2^+ + He^+ + He	**He*** + **He*** (or He_2*) →e + He_2^+ + He^+ + He
	In the Center	**He*** + e→ He^+ +2e	**He*** + **He*** (or He_2*) →e + He_2^+ + He^+ + He
	Close to Anode	**He*** + He + He → He_2* + He	**He*** + e→ He^+ +2e
He_2* lost	Close to Cathode	**He_2*** + **He_2*** (or He*) →e + He_2^+ + He^+ + He	**He_2*** + **He_2*** (or He*) →e + He_2^+ + He^+ + He
	In the Center	**He_2*** + **He_2*** (or He*) →e + He_2^+ + He^+ + He	**He_2*** + e→ He +He + e
	Close to Anode	**He_2*** + **He_2*** (or He*) →e + He_2^+ + He^+ + He	**He_2*** + e→ He +He + e

Table.4. Dominant generation processes by reaction for electrons, ions and metastables

Species	Discharge Position	P=250 Torr (For both low and high current cases)	P = 760 Torr (For both low and high current cases)
Electron gain	Close to Cathode	He + e → He^+ + **2e**	He + e → He^+ + **2e**
	In the Center	He* + e → He^+ + **2e**	He* (He_2*) + He* (He_2*) → **e** + He_2^+ + He^+ + He
	Close to Anode	He* (He_2*) + He* (He_2*) → **e** + He_2^+ + He^+ + He	He + e → He^+ + **2e**
He^+ gain	Close to Cathode	He + e → **He^+** + 2e	He + e → **He^+** + 2e
	In the Center	He* + e → **He^+** + 2e	He* (He_2*) + He* (He_2*) → e + He_2^+ + **He^+** + He
	Close to Anode	He* (He_2*) + He* (He_2*) → e + He_2^+ + **He^+** + He	He + e → **He^+** + 2e
He_2^+ gain	Close to Cathode	He^+ + He + He → **He_2^+** + He	He^+ + He + He → **He_2^+** + He
	In the Center	He^+ + He + He → **He_2^+** + He	He* (He_2*) + He* (He_2*) → e + **He_2^+** + He^+ + He
	Close to Anode	He^+ + He + He → **He_2^+** + He	He^+ + He + He → **He_2^+** + He
He* gain	Close to Cathode	He + e → **He*** + e	He + e → **He*** + e
	In the Center	He + e → **He*** + e	He_2^+ + e → **He*** + He
	Close to Anode	He_2^+ + e → **He*** + He	He + e → **He*** + e
He_2* gain	Close to Cathode	He* + He + He → **He_2*** + He	He* + He + He → **He_2*** + He
	In the Center	He* + He + He → **He_2*** + He	He* + He + He → **He_2*** + He He_2^+ + e + He → **He_2*** + He +e
	Close to Anode	He* + He + He → **He_2*** + He	He* + He + He → **He_2*** + He

2.4 Point measurements of gas temperatures (T_g) in a N_2 atmospheric pressure micro-discharge by rotational Raman spectroscopy.

A N_2 discharge at near-atmospheric pressure was operated in a 500 μm gap between Mo electrodes at DC currents of up to 30 mA. A pulsed Nd-YLF laser beam was focused in the gap with a novel miniature periscope. N_2 rotational Raman backscattered at 180° was collected in a confocal configuration. We constructed a triple grating monochromator with a spatial filter between the first and second gratings to drastically reduce scattered laser light and Rayleigh scattering. The optical system provided a spatial resolution of <100 μm. Sample spectra recorded with an intensified CCD are shown in Fig. 2.9. Laser scatter, recorded with no N_2 flow and the reactor evacuated, exhibits a dip near the center wavelength (near pixel #170) due to the spatial filter. The spectrum with 600 Torr N_2 and no discharge has extended wings that are due to ground vibronic state

rotational Raman scattering. When the discharge was ignited (blue curve in Fig. 2.10), the wings were broadened, due to scattering from higher rotational levels.

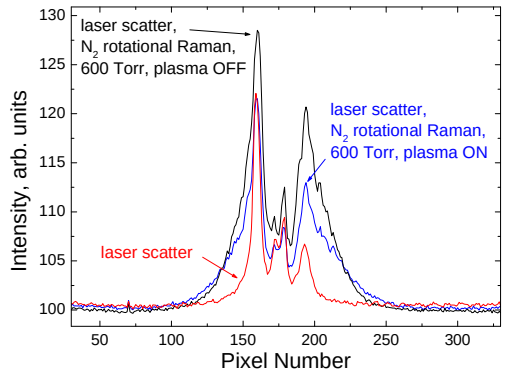

Fig. 2.9. Spectra recorded with the laser-Raman confocal microscope and triple monochromator.

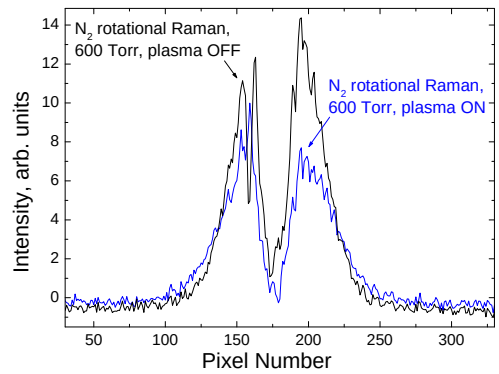

Fig. 2.10 Net rotational Raman spectra (laser scattered light subtracted off) with the plasma ON (24 mA) and OFF.

T_g was determined by matching experimental spectra to model spectra obtained by convolution of theoretical line intensities with the apparatus spectral resolution, with T_g as the adjustable parameter. T_g measurements as a function of pressure (P = 400 – 760 Torr) and discharge current (current density j_d = 200 – 1000 mA/cm^2) are shown in Fig. 2.11. Midway between the electrodes, T_g increased linearly with j_d, reaching 420 K at 1000 mA/cm^2 and 720 Torr. The magnitude of T_g and dependence on j_d are consistent with a dominant ion Joule heating mechanism. Also, the relative intensity of Raman scattering indicates a $1/T_g$ dependence on N_2 number density, and hence a negligible dissociation of N_2 even at the highest j_d.

2.5 T_g and electron densities in a He and Ar atmospheric pressure micro-discharge, measured by optical emission spectroscopy.

T_g in He and Ar slot micro-discharges were measured by adding small amounts of N_2 (<200 ppm) to the feed gas and recording N_2 C→B spectra (Fig. 2.12) as a function of gas flow rate. It was found that the rotational population of the N_2 C-state is in a Boltzmann equilibrium in atmospheric pressure He micro-discharges, but not in Ar. Energy transfer from Ar metastables to N_2 and electron impact excitation of N_2 result in two different rotational state distributions in N_2(C v=0,1,2). The rotational-to-translational (R-T) energy transfer is not fast enough to equilibrate the rotational distribution with the gas temperature. A two-temperature model was applied to simulate the N_2 C → B rotational spectra; T_g is the lower of these two temperatures. T_g for Ar and He micro-discharges are shown in Figs. 2.13 and 2.14.

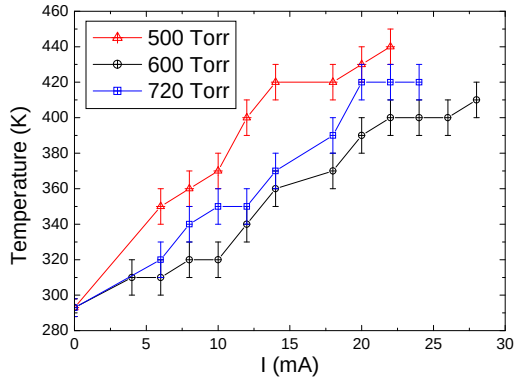

Fig. 2.11. T_g in a N_2 micro-discharge, determined from rotational Raman scattering, as a function of discharge current and pressure.

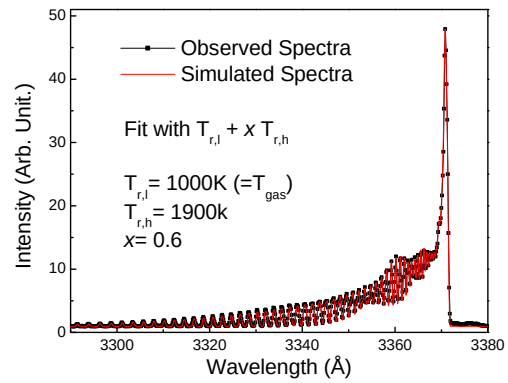

Fig. 2.12. N_2 C→B plasma-induced emission spectra in a mostly Ar micro-discharge.

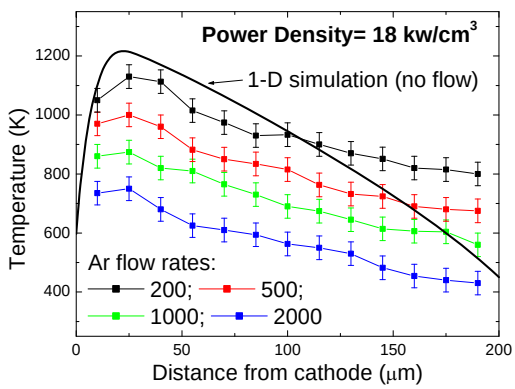

Fig. 2.13. T_g *vs.* distance from the cathode in an atmospheric pressure, mostly Ar micro-discharge, for various flow rates of feed gas through the discharge slot. Solid line is a simulation for no gas flow.

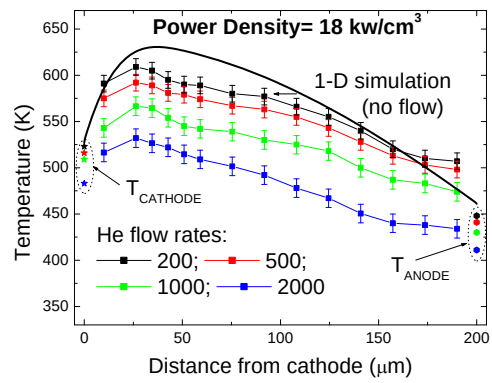

Fig. 2.14. T_g *vs.* distance from the cathode in an atmospheric pressure, mostly He micro-discharge, for various flow rates of feed gas through the discharge slot. Solid line is a simulation for no gas flow.

At 760 Torr and 18 kW/cm^3 power density, T_g in Ar micro-discharges was between 500 K and 1100 K, depending on position between the electrodes. At the same current and pressure, temperatures were much cooler (425 to 600 K) in He micro-discharges on account of the higher thermal conductivity of He. Electron densities were determined from the spectral line broadening of H-β emission. For example, electron densities for Ar micro-discharges in the bulk plasma region were 1.8 x 10^{14} cm^{-3} at 40 mA and 4.5 x 10^{14} cm^{-3} at 90 mA.

3. 2-D Numerical simulations

Models of DC He and Ar micro-discharges were developed and were used to compute 2-D electron densities, electron temperatures, T_g (Figs. 3.1 and 3.2), and other relevant parameters. T_g values were in excellent agreement with experimental measurements, both as a function of distance between the electrodes and as a function of

gas flow rate through the micro-discharge. T_g decreased with increasing gas flow due to convective removal of heat. T_g peaked off axis near the cathode as ions accelerated in the cathode sheath and deposited part of their energy in frequent collisions with the neutral gas.

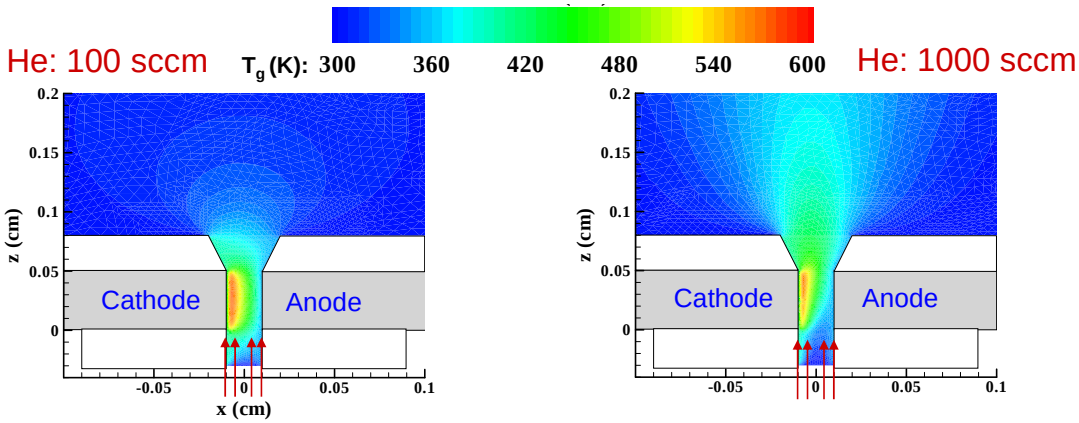

Fig. 3.1. Computed T_g in He Micro-discharges at 760 Torr. Power = 18 kW/cm^3.

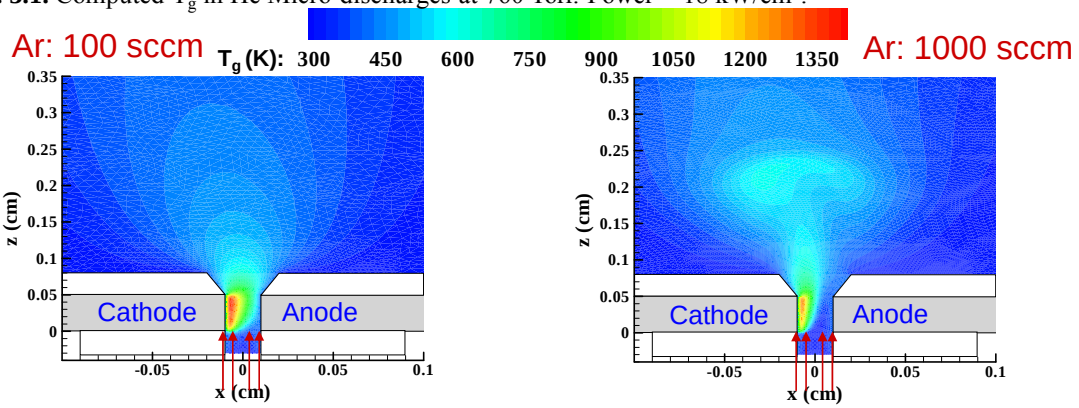

Fig. 3.2. Computed T_g in Ar Micro-discharges at 760 Torr. Power = 18 kW/cm^3.

4. Publications acknowledging support of this grant

S. G. Belostotskiy, O. Tola, V. M. Donnelly, D. J. Economou, and N. Sadeghi, "Gas Temperature and Electron Density Profiles in an Argon DC Microdischarge Measured by Optical Emission Spectroscopy," *J. Appl. Phys*. **107**, 053305 (2010) [7 pages].

S. G. Belostotskiy, V. M. Donnelly, D. J. Economou, and N. Sadeghi, "Spatially Resolved Measurements of Argon Metastable ($1s_5$) Density in a High Pressure Microdischarge Using Diode Laser Absorption Spectroscopy," *IEEE Trans. Plasma Sci.*, **37**, 852-858 (2009).

Sergey Belostotskiy, Vincent M. Donnelly, and Demetre J. Economou, "Influence of Gas Heating on High Pressure DC Microdischarge I-V Characteristics," *Plasma Sources Sci. Technol*., **17**, 045018 (2008).

Sergey Belostotskiy, Rahul Khandelwal, Qiang Wang, Vincent M. Donnelly, Demetre J. Economou, and Nader Sadeghi, "Measurement of Electron Temperature and Density in an Argon Microdischarge by Laser Thomson Scattering," *Appl. Phys. Lett*., **92**, 221507 (2008).

Q. Wang, F. Doll, V. M. Donnelly, D. J. Economou, N. Sadeghi, and G. Franz, "Experimental and Theoretical Study of the Effect of Gas Flow on Gas Temperature in an Atmospheric Pressure Microplasma," *J. Phys. D: Appl. Phys*., **40**, 4202-4211 (2007).

S. Belostotskyi, Q. Wang, V. M. Donnelly, D. J. Economou, and N. Sadeghi, "Three Dimensional Gas Temperature Measurements in Atmospheric Pressure Microdischarges Using Raman Scattering," *Appl. Phys. Lett*., **89**, 251503 (2007).

Q. Wang, D. J. Economou, and V. M. Donnelly, "Simulation of Direct Current Micro-Plasma Discharge in Helium at Atmospheric Pressure," *J. Appl. Phys*., **100**, 023301 (2006).

Q. Wang, I. Koleva, V. M. Donnelly, and D. J. Economou, "Spatially Resolved Diagnostics of a Direct Current Atmospheric Pressure Helium Micro-plasma," *J. Phys. D: Appl. Phys.*, **38**, 1690-1697 (2005).